CHAPTER 20

MOLECULAR AND SOLID C_{36}

JEFFREY C. GROSSMAN, CHARLES PISKOTI, STEVEN G. LOUIE, MARVIN L. COHEN, and ALEX ZETTL

20.1 INTRODUCTION

The synthesis and identification of the pure carbon-cage molecule C_{60} in 1985 [1] set the stage for a flurry of experimental and theoretical activity [2] catalyzed by the discovery of a bulk synthesis method [3]. In its molecular form, C_{60} is a highly spherical hollow-cage molecule with the carbon atoms in the shell arranged in a network of hexagons and pentagons. In the experimentally observed and energetically most favorable "soccer ball" configuration, all 12 pentagons are "isolated." The fact that C_{60} is the smallest fullerene obeying the isolated pentagon rule [4] has prompted some to suggest that it is in fact the smallest possible stable fullerene: smaller pure-carbon-cage molecules formed from hexagons and pentagons must necessarily contain adjacent pentagons with a resultant large strain energy. While the exceptional stability of C_{60} is undisputed, the impossibility of stable "lower-order" fullerene-like molecules and molecular solids formed from such carbon networks is by no means a foregone conclusion. Indeed, such structures, precisely because of their enhanced strain energy and higher chemical reactivity, might be expected to display chemical, electronic, magnetic, and mechanical properties significantly different from (and possibly technologically more important than) those of the more conventional fullerenes.

Recent theoretical and experimental work [5–10] has shown that C_{36} is a stable carbon-cage molecule and is the basis of novel pure-carbon solids. Both the molecule and the solid display a rich spectrum of physical properties. We here summarize recent research progress on this interesting new material.

Pseudopotential density functional calculations show that the structure with D_{6h} symmetry is one of two most energetically favorable. Based on this result and the fact that D_{6h} is conducive to forming a periodic system, a new solid

Fullerenes: Chemistry, Physics, and Technology, Edited by Karl M. Kadish and Rodney S. Ruoff.
0-471-29089-0

phase of carbon using C_{36} fullerenes as a basis is proposed. The lowest energy crystal is a highly bonded network of hexagonal planes of C_{36} units with AB stacking. The electron–phonon interaction potential for C_{36} is substantially enhanced compared to C_{60}, leading to the possibility of larger superconducting transition temperatures than in alkali-doped C_{60} solids. The reaction pathway to form a neutral C_{36} dimer is predicted to be barrierless, while negatively charged C_{36} molecules are less likely to bond due to a substantial barrier of formation. Calculations on doping demonstrate that substitutional doping with nitrogen can lead to a 10% decrease in the C–C bond lengths of C_{36}. Calculated endohedral binding energies show that C_{36} is perhaps the smallest fullerene size that can easily trap a range of atoms. For the lowest-energy solid, it is predicted that Na is the largest alkali atom that can be intercalated into the new crystal structure without causing severe structural distortion. Further molecular properties, such as nuclear magnetic resonance (NMR) chemical shifts and infrared (IR) absorption spectra, are evaluated for the two lowest-energy fullerene isomers. It is shown that these isomers are sufficiently different chemically to distinguish by these methods.

Although evidence for isolated C_{36} molecules can be inferred from early gas-phase carbon studies [11–13], it is only recently that bulk quantities of C_{36} have been obtained using variations on the original Krätschmer–Huffman arc-plasma technique [3]. The molecular form of C_{36} has been investigated via mass spectroscopy, and bulk solids have been studied experimentally via electron diffraction, transport measurements, and scanning tunneling spectroscopy. Electron diffraction suggests that C_{36} forms a closed-packed solid with a lattice constant significantly smaller than that of the C_{60} counterpart. In contrast to solids formed from C_{60} and higher-order fullerenes, the C_{36} solid is not a purely van der Waals solid but has covalent-like bonding, leading to a solid with enhanced structural rigidity. Tunneling spectroscopy gives evidence for clustering of C_{36} molecules, where the clusters retain energy level signatures of the original molecular orbitals. Alkali doping increases the conductivity of C_{36} and helps dissociate the solid into molecular units under laser irradiation.

20.2 METHODS

Calculations on solids reported in this chapter have been carried out using a plane wave pseudopotential total-energy scheme [14]. We employ the local density approximation [15,16] and use the Ceperley–Alder interpolation formula [17] for the exchange-correlation energy. Ab initio pseudopotentials are generated using the method of Martins et al. [18] and include semirelativistic corrections. Irreducible k-points are generated according to the Monkhorst–Pack scheme [19], and convergence is tested for each solid and is achieved with a range of 6–27 k-points in the irreducible part of the Brillouin zone, depending on the crystal structure. As energy cutoff of 60 Ry is used for the carbon atoms to ensure convergence in the total energy to less than 1 mRy per atom. For all

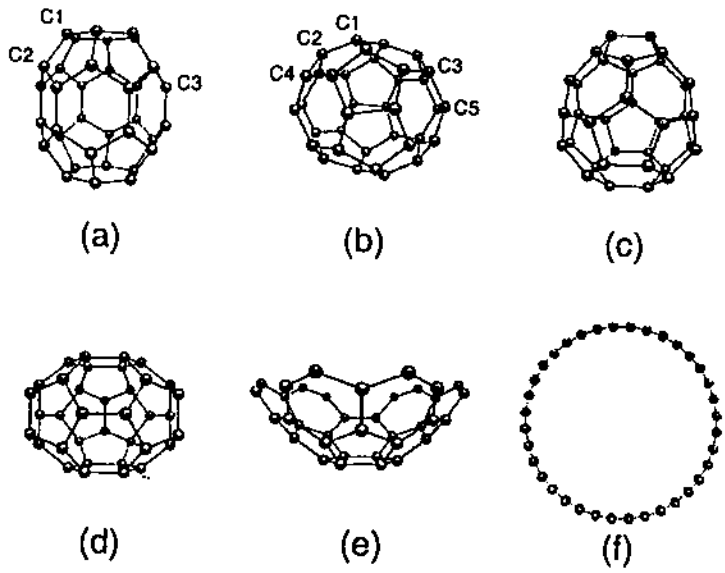

Figure 20.1 Six structural isomers of C_{36}: (a) the D_{6h}, (b) D_{2d}, (c) C_{2v}, and (d) D_{3h} fullerenes, (e) the C_{3v} bowl, and (f) the D_{18d} ring. Symmetry unique atoms are labeled for the first two structures.

molecular calculations, electronic and structural properties are calculated with DMol version 960 [20] using the frozen-core approximation, a fine integration grid mesh, and double numerical plus polarization basis sets. Both the local density [21] and generalized gradient [22,23] approximations (LDA and GGA) are used.

20.3 MOLECULAR PROPERTIES

20.3.1 Structures

The 36-atom carbon clusters lie in an interesting size regime, intermediate between the fullerene ($N = 40$–90) and ring ($N = 10$–28) dominated sizes. Five distinct peaks are observed in mobility measurements [24] of pure C_{36} isomers, corresponding to fullerenes, rings, and planar graphite-like structures. Theoretical mobility studies [25] matched several of these peaks very well, although it is not possible to distinguish among the fullerenes using mobility measurements alone. Here we consider six distinct equilibrium structures (see Fig. 20.1): the D_{6h}, D_{2d}, C_{2v}, and D_{3h} fullerenes, a corranulene-like bowl (C_{3v}), and a monocyclic ring (D_{18d}). Eleven other classical fullerene structures exist for 36 atoms [26]; however, most of these are less likely to form due to the considerable strain caused by clustering too many pentagons next to one another.

TABLE 20.1 Energy Differences (eV) Within the LDA and GGA (B-PW91) Methods for Five C_{36} Isomers, Relative to the D_{6h} Fullerene[a]

	Fullerenes				Bowl	Ring
	D_{6h}	D_{2d}	C_{2v}	D_{3h}	C_{3v}	D_{18d}
LDA	0.0	0.0	0.5	1.4	9.5	11.6
BPW91	0.0	0.0	0.5	1.8	7.1	20.3
Δ	0.5	0.4	0.4	0.4	2.0	0.5
EA	−3.3	−3.0	−3.3	−3.4	—	—

[a] Each structure has been fully relaxed within the given symmetry by both methods. LDA HOMO–LUMO gaps (Δ) and electron affinities (EA) are also given.

20.3.2 Energetics

For the six geometries of Figure 20.1, full structural relaxations within the given symmetries have been carried out using both LDA and GGA. Total energy differences for these structures are listed in Table 20.1. We find the fullerenes to be substantially more stable than the bowl and the ring, in agreement with previous theoretical studies [27]. Our calculations predict the D_{6h} and D_{2d} fullerenes to be the most energetically favorable structures and to be essentially isoenergetic.

As seen in Table 20.1, there is a ~0.25 eV/atom difference between LDA and GGA in predicting the ring–cage energy differences. This is consistent with previous results, which indicated that LDA is a poor predictor when comparing carbon structures with dramatically different bonding character [28,29]. Indeed, the energy differences between the four fullerene structures, which have essentially identical bonding character, are very similar for LDA and GGA. In contrast to the calculations for C_{20} isomers, this case does not appear to require further, more accurate calculations by, for example, quantum Monte Carlo approaches, since for C_{36} discrepancies between the LDA and GGA do not qualitatively change the energetic ordering of the structures.

In addition to total energies, we compute LDA gaps between highest occupied and lowest unoccupied molecular orbitals (HOMO–LUMO) as well as electron affinities (see Table 20.1). The four fullerenes all have roughly the same HOMO–LUMO gap and similar electron affinities. Note that for each fullerene, an additional electron is well bonded to the molecule, as is the case for many of the intermediate-size carbon fullerenes. The remainder of this chapter focuses on the two lowest-energy structures as they are likely to be more abundant and easier to synthesize experimentally.

Of the two lowest-energy structures, the higher symmetry (D_{6h}) structure can form simple solids and will therefore be the main focus of the rest of this chapter. The C_{36} (D_{6h}) is a good prototypical system for our theoretical study since it is small yet highly symmetric. Furthermore, the D_{6h} structure has the advantage that higher degeneracy in the electronic levels, because of its higher

symmetry, can lead to a potentially large density of states. Later in this chapter, we will discuss possible means for distinguishing it from the D_{2d} structure.

20.3.3 D_{6h} C_{36}

The relaxed D_{6h} C_{36} structure has a height of 5.2 Å and a width of 4.9 Å as measured from the atomic positions. Any closed structure consisting of three-fold coordinated atoms that form only pentagons and hexagons must have 12 pentagons according to Euler's relations. In the D_{6h} structure, the pentagons form two belts around the top and bottom hexagons and there is a row of hexagons separating these pentagon belts (Fig. 20.1a).

The calculated LDA binding energy is 8.14 eV/atom for this structure, compared with C_{60}, which has a binding energy of 8.42 eV/atom within the same method. This result shows that, as expected due to its smaller size, there is a higher energy cost per atom in forming the C_{36} cage than C_{60}. In fact, most of the energy cost in forming C_{60} can be attributed to the strain energy involved in curving the structure. It is possible to estimate this strain energy by considering the deviation of the π-orbital axis vector (POAV) from the planar configuration [30–32]. In its simplest form, the POAV is defined as the vector that makes equal angles ($\theta_{\sigma\pi}$) to the three σ bonds at a conjugated carbon atom. A simple formula for estimating the strain energy is obtained using a fit to a set of carbon molecules [32]:

$$E_{\text{strain}}(\text{eV/atom}) \approx 8.7 \frac{1}{N} \sum^{N} (\theta_{\sigma\pi} - \pi/2)^2$$

where the angle is expressed in radians. The quantity $(\theta_{\sigma\pi} - \pi/2)$ can be evaluated from the structure and for C_{60} it is found to be 11.64°. Using the above formula, C_{60} is estimated to have a strain energy of 0.36 eV/atom, which accounts for most of the energy difference between its binding energy and that of graphite (8.86 eV/atom within this method). The D_{6h} C_{36} structure has three nonequivalent atoms, labeled in Figure 20.1. For the C1, C2, and C3 sites, the quantities $(\theta_{\sigma\pi} - \pi/2)$ are found to be 17.10°, 16.01°, and 12.82°, respectively. Using the above equation, we obtain an estimate for the strain energy of 0.62 eV/atom, which is in very good agreement with our LDA calculated energy difference relative to graphite. Thus, as in C_{60}, the energy required to form C_{36} is due to the hybridization caused by curvature. Since clustering of pentagons creates severely strained atomic sites, it is preferable for the pentagons to be spread over the whole structure as in the case of the D_{6h} and the D_{2d} fullerenes. The values of the $\theta_{\sigma\pi}$ angles also suggest that the C1 and C2 atoms should be the most reactive sites in this structure.

In Figure 20.2 we show the energy levels near the Fermi gap. The calculated energy gap is found to be 0.5 eV between singlet states of representation B_{1u} and B_{2g} for the occupied and unoccupied state, respectively. One should keep in

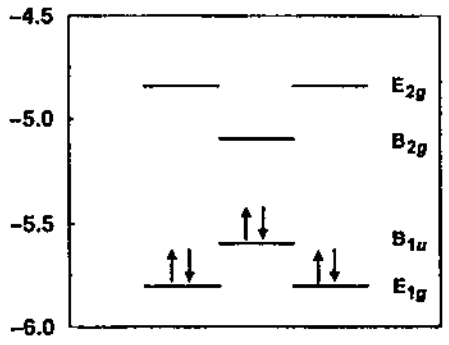

Figure 20.2 Energy levels of the D_{6h} structure near the Fermi energy. We show here the last two sets of occupied states and the first two sets of unoccupied states.

mind that the LDA has the tendency to underestimate the real gap of a structure. The second to last occupied states and next unoccupied states above the singlet are both part of doublets with symmetry E_{1g} and E_{2g}, respectively.

20.4 DIMER FORMATION

As a first step toward building a C_{36} solid, we have investigated the possibility of intermolecular bonding through a series of calculations for a variety of C_{36} dimers and trimers [9]. All geometries are fully relaxed within the given symmetries. Dimerization was tested at each of the three nonequivalent sites of the C_{36} molecule, with either one or two single bonds between two C_{36} molecules. Stable dimer formation occurred between C atoms located on the top hexagon or on the pentagon ring (C1 and C2 of Fig. 20.1a), but not for the third nonequivalent site on the middle hexagon belt (C3). In fact, completely unbonded dimers resulted from the latter case.

Figure 20.3 depicts three of the different dimers—$(C_{36})_2$-A, $(C_{36})_2$-B, and $(C_{36})_2$-C (hereafter referred to as dimers A, B, and C)—and one of the trimers, $(C_{36})_3$, considered in this chapter. Below each unit is the relevant symmetry and calculated binding energy. In all cases, the intermolecular bond distances can be considered as single C–C covalent bonds with an average length of 1.56 Å. Bonding that involves sites on the pentagon ring appear more favorable than bonding involving atoms on the top hexagon sites, but all of the configurations shown are energetically bound with respect to isolated molecules. Note that dimer C, which is the most stable configuration, can be obtained from dimer B simply by rotating one of the C_{36} units with respect to one another without breaking an existing bond.

Given the potential for C_{36} molecules to bond to one another, we investigate the reaction pathway for the formation of a C_{36} dimer [10]. We choose dimer C,

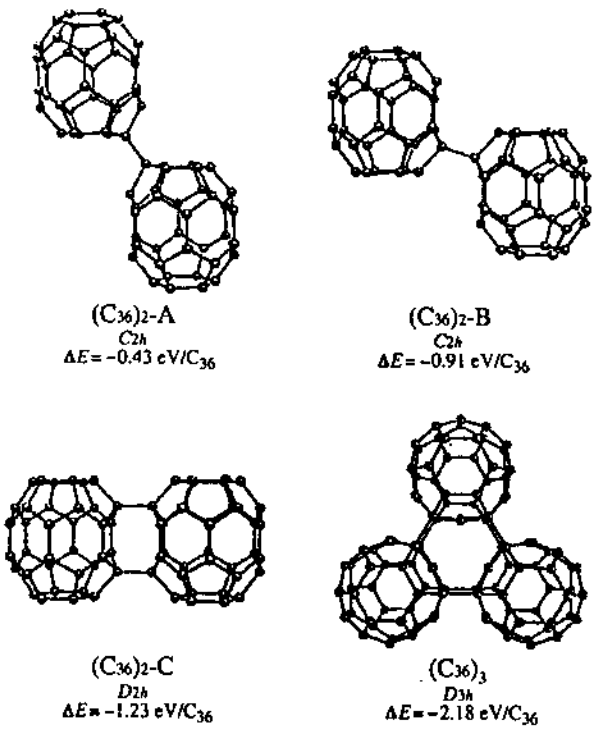

Figure 20.3 Three different configurations of C_{36} dimers, and a C_{36} trimer, with their corresponding symmetries and binding energies with respect to isolated C_{36} molecules. To clarify the structure of the trimer, the z axis has been rotated.

which is also the lowest energy dimer according to our calculations. The reaction coordinate is along the C_{36}–C_{36} bond axis.

In Figure 20.4 we show the results of our LDA total energy calculations for varying intermolecular separations. At each point, a full structural optimization is carried out with the constraint of fixed intermolecular bond distance. As the molecules are brought closer together, the onset of an attractive, van der Waals type of interaction appears at around 4.5 Å and possesses a minimum at about 3.0 Å. At about a 2.6 Å separation, a small barrier of ~0.1 eV is encountered before the dimer begins to covalently bond (reaching a stable minimum at 1.6 Å). Thus, the LDA calculations imply an effectively barrierless dimerization reaction since the peak of the barrier encountered remains below the initial reactant energies.

The appearance of a kink in the reaction path may imply that the reaction induces a change in the molecular state symmetry. The LDA approach is a single-determinantal method and therefore cannot represent such a symmetry crossing accurately. However, qualitatively the results would not change since

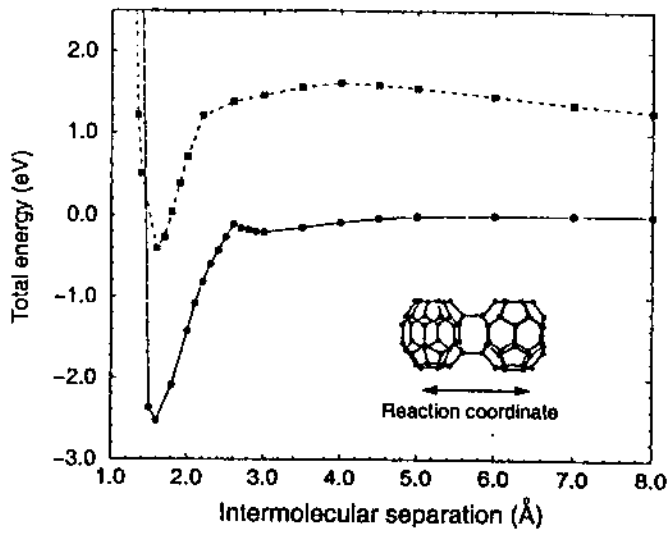

Figure 20.4 Calculated lowest energy reaction pathways of C_{36} dimer formation for both neutral (circles) and negatively charged (squares) species. The reaction coordinate is along the intermolecular bond axis as shown. The neutral and charged curves have been shifted by twice the total energy of the isolated C_{36} and C_{36}^- molecules, respectively.

the barrier occurs below the reactant energy and the only difference would be to smooth out the kink in question.

Previous ab initio calculations for C_{60} dimer formation did not include structural relaxation at each point on the reaction path and are therefore difficult to compare with the present calculations. In the work of Adams et al. [33], LDA total energy calculations were carried out on interpolated C_{60} dimer coordinates and a barrier of 2.2 eV was found. Experimentally, it is well known that undoped C_{60} has to be photoexcited or treated at high pressure to polymerize, whereas alkali-doped C_{60} tends to polymerize spontaneously. Our calculations suggest that spontaneous polymerization for C_{36} is highly likely *without* doping. The strong dimer binding of 2.6 eV for C_{36} (compared with 0.6 eV for our calculations of the C_{60} dimer binding) lends further credence to the idea that C_{36} naturally prefers to polymerize.

As an additional comparison with C_{60}, we have evaluated total energies along the reaction path for C_{36}^- molecules (such that the dimer has a charge of -2). These results, shown as squares in Figure 20.4, indicate that the presence of charge may substantially inhibit dimer formation. The two negatively charged molecules experience an electrostatic $1/r$ repulsion as they approach one another, which accounts for the fact that at 8 Å separation the dimer is more than 1 eV unbounded. At the equilibrium distance of 1.6 Å the charged system is energetically bound by roughly 0.4 eV; however, to reach this minimum the system must pass through an unfavorable barrier, which is 0.35 eV

above the energy at 8 Å separation and 1.5 eV above the energy of two isolated C_{36}^- molecules. Therefore, we propose that it may be necessary and desirable to provide a source of negative ions in order to prevent C_{36} molecules from bonding to one another. The opposite is true in C_{60}, for which it has been shown both theoretically and experimentally that negative ions lower the barrier to dimerization and significantly enhance polymerization [33–35].

20.5 SOLID PROPERTIES

The originally proposed C_{36} solid [6] was formed using a rhombohedral crystal lattice because it involved only one C_{36} molecule per unit cell and was therefore computationally less demanding. Subsequently, we found that a very similar crystal, but with hexagonal symmetry imposed, was substantially lower in energy and had completely different electronic properties [7]. In particular, our calculations of the density of states (DOSs) revealed that the rhombohedral crystal is metallic with a large peak at the Fermi energy (E_F), whereas the hexagonal crystal is insulating with a large gap of ~2 eV. Furthermore, the hexagonal structure was found to have a significantly larger binding energy per molecule than the rhombohedral crystal.

The difference between these crystals is perhaps best understood by considering that each is simply a stacking of hexagonally symmetric planes of well-separated C_{36} units. Figure 20.5 shows the two kinds of stacking sequences—AB and ABC—corresponding to the hexagonal and rhombohedral crystals, respectively. In each case, both a top view of the repeating planes and a side view showing relaxed interlayer bonding character are shown. The fundamental stacking unit is a plane of unbonded C_{36} molecules, which we refer to as sheet 1 (S1), and the two crystals are labeled S1-AB and S1-ABC for the two kinds of stacking. The AA stacking sequence (i.e., S1-AA) is not considered here because it does not form a metastable structure, as will be discussed later.

In Table 20.2 we list the binding energy, density, gap, and k-point sampling for each of these crystals. The same information for a single S1 sheet is also given, although these data simply correspond to an isolated C_{36} molecule since the C_{36} units are essentially noninteracting within an S1 sheet. Note the dramatic differences in electronic and structural properties, despite the fact that the densities are roughly the same. The S1-ABC crystal has a binding energy of 3.53 eV/C_{36}, which is larger than our previous result of 2.2 eV/C_{36} [6] for this crystal. The difference is due to k-point convergence: In the present study we employ a $5 \times 5 \times 5$ shifted grid (23 k-points in the irreducible part of the Brillouin zone) whereas in the previous calculation we used a $3 \times 3 \times 3$ shifted grid (6 k-points) for structural relaxation. Here, structural and energetic properties are fully converged with respect to k-points separately for each crystal.

Interestingly, the significant differences in electronic properties between S1-ABC and S1-AB can be reproduced in isolated $C_{36}H_6$ molecules, where the H atoms are attached to the same six sites of adjacent interlayer bonds in the

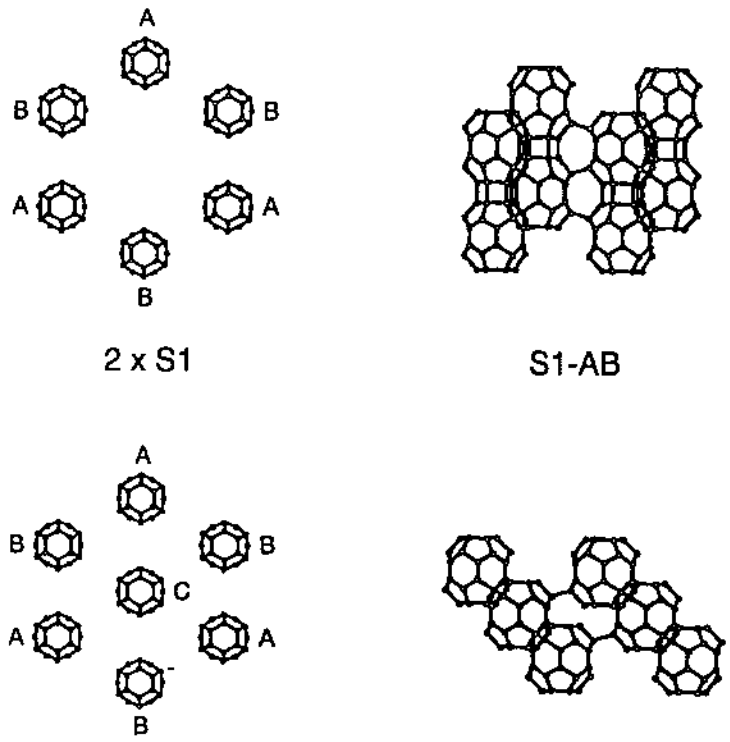

Figure 20.5 Fully relaxed LDA crystal structures formed by stacking planes of unbonded C_{36} units. For the two different stacking types a top view (*left*) shows the repeating planes and a side view (*right*) shows interlayer bonding.

TABLE 20.2 Binding Energy (eV/C_{36}), Density (C_{36}/au^3), and Gap (eV) for Each Crystal Considered Here[a]

Structure	Binding	Density	Gap	*k*-Point Grid
S1	0.00	—	0.50	$1 \times 1 \times 1$
S1-AB	6.92	0.49	1.95	$5 \times 5 \times 5$
S1-ABC	3.53	0.51	metal	$5 \times 5 \times 5$
S2	1.67	—	1.09	$6 \times 6 \times 1$
S2-AA	3.98	0.72	0.86	$5 \times 5 \times 5$
S2-AB	7.71	0.76	0.61	$4 \times 4 \times 4$
S2-ABC	1.84	0.63	0.15	$4 \times 4 \times 4$

[a] S1/S2 correspond to sheets without/with intralayer bonding. *k*-Point grids used for each calculation are also given. For reference, our calculated binding energy of isolated C_{36} is 8.14 eV/atom.

crystals. Upon structural relaxation, we find that D_{3d} $C_{36}H_6$ has a large gap of 2.2 eV and is energetically favored by 3.1 eV over D_{3h} $C_{36}H_6$, which has a much smaller gap of 0.4 eV.

The D_{3d} symmetry form disrupts all six aromatic rings in the belt of six fused benzenes and the D_{3h} form disrupts only alternate benzene rings. However, our calculations for various dihydrogenated forms of C_{36} show that simple resonance concepts that accurately predict the hydrogenation pattern in small polyacenes do not explain the results seen for C_{36}. This could be the case either because the action of resonance stabilization is not valid in such fused ring systems, or because other effects such as ring strain are counteracting the expected resonance pattern. A clear understanding of the difference between these two simple hydrogenated C_{36} molecules should also explain the difference between S1-ABC rhombohedral and S1-AB hexagonal C_{36} crystals. A thorough study of hydrogenation patterns in C_{36} and its component fragments, including the determination of overall strain and resonance energies by considering homodesmotic reactions, is discussed by Colvin et al. [36].

As we showed in the preceding section, the D_{6h} C_{36} molecules form stable dimers and trimers with two intermolecular bonds for the dimer and six intermolecular bonds for the trimer (i.e., dimer C and the trimer in Fig. 20.3). Furthermore, C_{36} molecules may be added in the same manner to form an infinite sheet of bonded units [10]. We refer to this layer as sheet 2 (S2) and note that our calculations give a binding energy for such a sheet of 1.67 eV/C_{36} (see Table 20.2). In Figure 20.6 we show a top view of S2 as well as side views of three different relaxed crystal structures, which form by stacking S2 layers according to AA, AB, or ABC sequences. All three stacking types lead to energetically bound layers.

For S2-AA, there is bonding between all six C atoms of the hexagon rings on top and bottom, as in the case of S1-AB. Such a stacking scheme therefore leads to intermolecular bonds for 24 of the 36 C atoms in each molecule. As shown in Table 20.2, S2-AA has a much higher density than the structures based on S1. Nonetheless, its binding energy is only slightly larger than that of S1-ABC and still 3 eV/C_{36} less than the binding of S1-AB.

Stacking S2 sheets in the AB sequence results in a slightly larger density and a substantially larger binding energy than S2-AA. In fact, S2-AB is the lowest energy crystal structure we have studied to date. It has the same number of intermolecular bonds as S2-AA and a d-spacing of 6.55 Å.

The S2-ABC crystal structure contains no interlayer bonding and has a much smaller total binding energy (1.8 eV/C_{36}) than the other solids. Since the interlayer binding is <0.2 eV/molecule, it should be rather easy for sheets stacked in this manner to "slip" over one another into the much more energetically favorable AB stacking scheme. Thus, we believe that the S2-ABC solid is unlikely to remain stable.

In Figure 20.7 we show the electronic density of states for the lowest energy (S2-AB) structure. Note that the crystal has characteristics typical of a molecular solid, with large peaks in the range of 10–20 states and narrow widths of

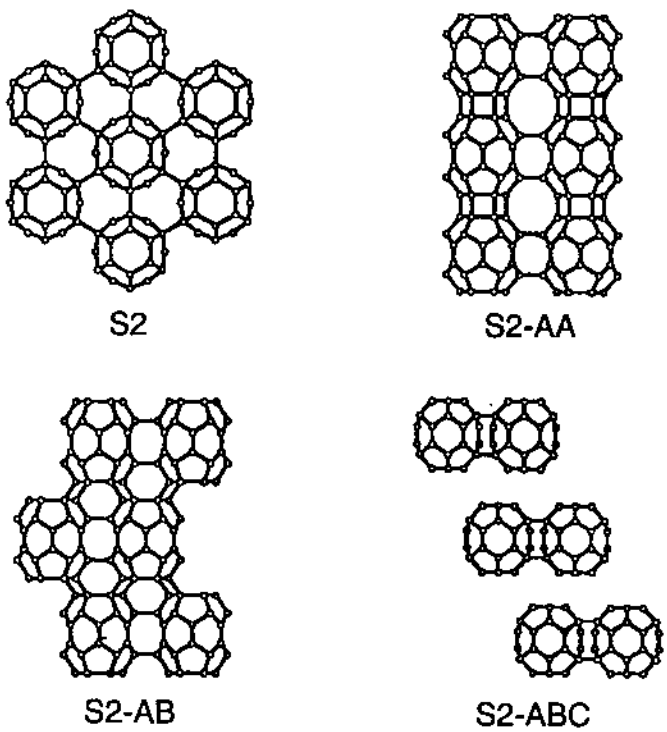

Figure 20.6 Fully relaxed LDA crystal structures formed by stacking planes of bonded C_{36} units. A representative S2 sheet (top view) and side views of three stacking types shows intra- and interlayer bonding, respectively.

less than 0.5 eV. The large, isolated peaks just above and below E_F account for roughly two electrons, which implies that half-filling of a band can be achieved through electron/hole doping with 1 electron donor/acceptor per C_{36}.

20.6 SUPERCONDUCTIVITY

It has been argued that the curvature of the C_{60} fullerene is thought to be responsible [37,38] for the substantial increase in T_c in its solid phase compared to intercalated graphite. Since C_{36} is even more curved than C_{60}, this argument is suggestive of even higher transition temperatures in C_{36}-based solids. To explore this possibility, we have carried out state of the art calculations of the electron–phonon interaction potential, V_{ep}, which is used in the definition of the coupling parameter $\lambda = N(0)V_{ep}$, where $N(0)$ is the DOSs at E_F.

One can extract V_{ep} from the electron–phonon spectral function [39], which is a double average over the Fermi surface connecting states due to the change in the potential caused by a phonon. For fullerene crystals, the computation is

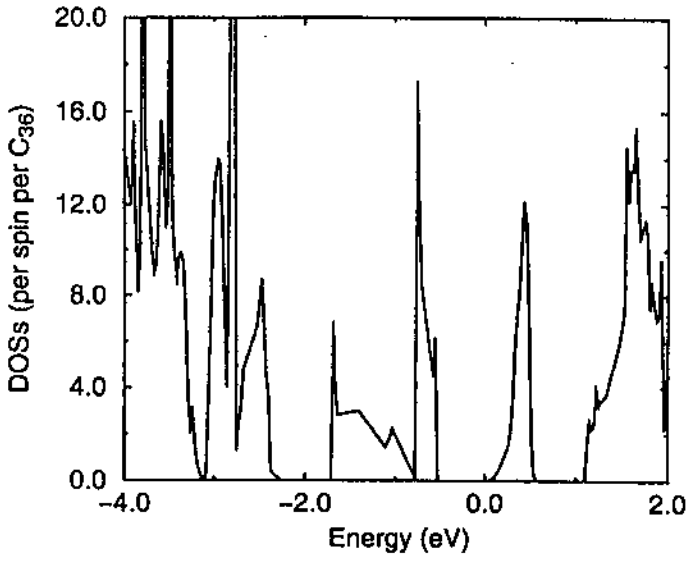

Figure 20.7 Calculated density of states (DOSs) for C_{36} crystal structure S2-AB. The Fermi energy is at 0 eV.

greatly simplified because of the small dispersion in both the electronic and phononic spectra. Therefore, one can use the electronic states and vibrational modes of the isolated molecule to approximate those found in the solid [38,40,41]; this implies that only the intramolecular modes are considered in the evaluation of V_{ep}. In the case of solid C_{36}, because of the intermolecular covalent bonds, one should carry out the full average over the Fermi surface. While such a calculation is prohibitive in practice, the C_{36} crystal appears to have molecular-like features, and we therefore use the procedure described above for the calculation of V_{ep}. However, the presence of covalent bonds in the crystal can cause the states of the isolated C_{36} molecule to rearrange and possibly mix in the solid. In order to keep our results as general as possible, we evaluate V_{ep} for the four molecular states that are nearest in energy to E_F.

The dynamical matrix is constructed using the forces on the atoms where only nonequivalent atoms are moved along the three Cartesian directions, and the rest of the information is obtained from the symmetry properties of this matrix. Diagonalizing the dynamical matrix yields the $3N$-dimensional polarization vectors, ε_α, with normalization $\varepsilon_\alpha \cdot \varepsilon_\beta = \delta_{\alpha\beta}$, which means that we have to use the DOSs per unit cell in the expression for λ. Using the approach outlined in the preceding paragraph, one can write

$$V_{ep} = \sum_\alpha \frac{1}{M\omega_\alpha^2} \frac{1}{g^2} \sum_{i,j=1}^{g} |\langle i|\varepsilon_\alpha \cdot \nabla V|j\rangle|^2 \tag{20.1}$$

TABLE 20.3 Electron–Phonon Coupling for the D_{6h} C_{36} Molecule[a]

Electronic States	Phonons Coupled	V_{ep} (meV)
E_{2g}	A_{1g}	32
	E_{2g}	154
B_{2g}	A_{1g}	136
B_{1u}	A_{1g}	126
E_{1g}	A_{1g}	39
	E_{2g}	120
$T_{1u}(C_{60})$	A_g	8
	H_g	63 (52[38], 56[40], 68[44], 49[45])

[a]States within 1 eV of the Fermi level are considered and the corresponding phonons that contribute to the electron–phonon interaction potential V_{ep} (see Eq. (20.1)) are listed. For each state, we list calculated values of V_{ep} (meV) for the given phonon modes. For comparison, the last row shows the same quantities calculated for A_3C_{60} with previous LDA results listed in parentheses.

where M is the mass of a carbon atom, i and j are degenerate electronic states in the isolated molecule for which we are evaluating the coupling, and g is the degeneracy of these states. The quantity $\langle i|\varepsilon_\alpha \cdot \nabla V|j\rangle$ is obtained by means of a finite difference approach. The application of selection rules to the matrix elements can be used as a consistency check to determine which vibrational modes should produce nonzero contributions. Within the LDA framework, we make no approximations or fits in our evaluation of V_{ep}.

Table 20.3 lists our calculated electron–phonon coupling values for several electronic states near E_F. The couplings due to the different phonon modes are listed separately since the A_g contribution to V_{ep} is expected to be screened out in A_3C_{60}. This effect has been observed by Raman scattering experiments [42,43] as well as demonstrated theoretically within the random phase approximation for static screening [44].

Our results for C_{60} are in good agreement with previous LDA calculations [38,40,44,45]. The results show that the coupling in C_{36} is substantially larger than in C_{60} for the E_{1g} and E_{2g} degenerate states. The increase in V_{ep} for C_{36} supports arguments based on curvature. Note that, although the A_g phonon modes comprise a slightly larger percent contribution of V_{ep} for C_{36} than for C_{60}, even without the inclusion of these modes the coupling strength of the E_{2g} electronic state is still enhanced by more than a factor of two compared with C_{60}. Of course, for the singly degenerate B_{2g} and B_{1u} states, removal of the contributions from A_g phonons would reduce the coupling to zero. The strongest coupling, both with and without the A_g contributions, is due to the doublet electronic states.

The strength of the electron–phonon interaction potential plays a crucial role in determining the superconducting transition temperature. Thus, our results imply that T_c in solid C_{36} can be significantly different than in solid C_{60}. The evaluation of T_c also requires knowledge of $N(0)$ and μ^*, which describes the Coulomb electron–electron repulsion. As we have shown, $N(0)$ for the solid

C_{36} considered here is expected to be comparable to that of doped C_{60}. Very recent experimental evidence suggests that μ^* is about 0.25 for A_3C_{60} compounds [46]. We may expect μ^* for C_{36} to be close to this value since the range and width of narrow subbands near the Fermi level and typical phonon energies are similar. However, due to the sensitivity of T_c to μ^* and the fact that μ^* is not known for C_{36}, only a very qualitative comparison of T_c can be made here. As an example, if we choose the same $N(0)$ and μ^* for C_{60} and C_{36}, such that $T_c = 18$ K for C_{60}, then a solution of the Eliashburg equations yields $T_c(C_{36}) \approx 6T_c(C_{60})$.

20.7 EFFECTS OF DOPING

20.7.1 Substitutional Doping

Substitutional doping of atoms on the fullerene cages by electron donors and acceptors such as N and B is of considerable interest because of induced changes in the electronic and structural properties of these molecules. Experimental evidence for the existence of N-doped C_{60} and C_{70} fullerenes has been verified by several groups [47,48], and theoretical studies have shown that both N and B can be substituted to form stable structures [49,50].

We have explored several N substitutionally doped C_{36} D_{6h} cages: $C_{34}N_2$, $C_{28}N_8$, and $C_{24}N_{12}$. In all cases no two dopant atoms are placed next to one another due to the strong nitrogen dimer bond, which weakens the overall structural integrity of the ball. This effect was tested for $C_{34}N_2$, where it was found that placing the N atoms next to one another decreases the total binding energy by ~3 eV compared with the cases where the two N atoms are apart. As the fullerene is further substituted with N, the positions of the nitrogen atoms become more important. Our calculations indicate that the most symmetric configurations are also the most energetically favorable. The highest symmetry case is $C_{24}N_{12}$, which can retain the full D_{6h} symmetry of the undoped molecule.

Upon structural relaxation, we find that the C–N bonds shorten by 2–3% with respect to the C–C bond lengths, in agreement with previous calculations on $C_{59}N$ [49]. A comparison of the four unique bond lengths of the D_{6h} $C_{24}N_{12}$ structure is given in Table 20.4. Interestingly, for the highest symmetry D_{6h}

TABLE 20.4 Comparison of the Four Unique Bond Distances (Å) in D_{6h} C_{36} and $C_{24}N_{12}$[a]

	d_1	d_2	d_3	d_4
C_{36}	1.41	1.48	1.43	1.43
$C_{24}N_{12}$	1.39	1.44	1.45	1.33

[a] All values are for fully relaxed LDA structures. The d_4 bond corresponds to the C–C bond across the hexagon belt (see Fig. 20.9).

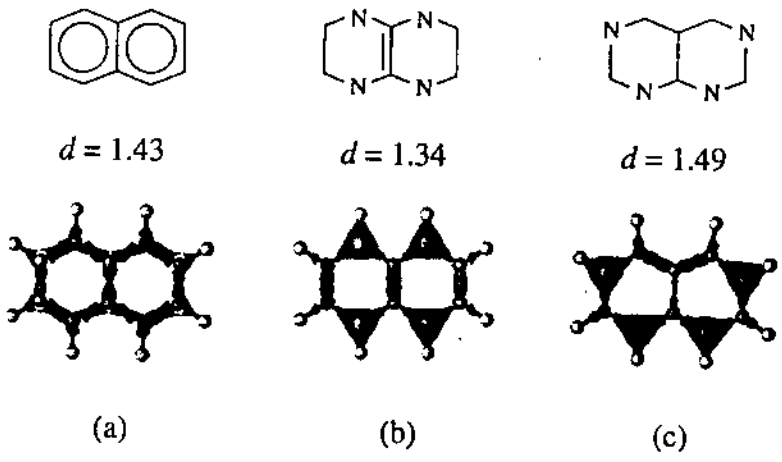

Figure 20.8 Planar $C_{10}H_8$ and $C_6N_4H_8$ molecules, shown with the total charge density and hydrogen atoms on bottom. The top figures illustrate the positions of the nitrogen atoms. The C–C distance of the center vertical bond is given for each case.

case, substitution with nitrogen results in a 10% shortening of the carbon–carbon bonds across the hexagon belt.

In order to understand better this effect, which causes the fullerene to possess six C–C double bonds, we consider the smaller, planar molecule $C_{10}H_8$. Figure 20.8 shows this test molecule for the case of (a) pure carbon and (b,c) two different configurations substituted with four nitrogen atoms. Total electronic charge densities are overlayed on each molecule in order to see more clearly the bonding character. The middle C–C bond (without any hydrogens and whose value is listed above each figure) represents the d_4 bond in the D_{6h} C_{36} and $C_{24}N_{12}$ fullerenes. In the pure carbon case this bond is 1.43 Å, which is exactly what it is in pure C_{36}. Upon introducing the nitrogen (Fig. 20.8b), the middle bond shortens to 1.34 Å, which is similar to the reduction in d_4 seen in the N-substituted fullerene. Note, however, that if the nitrogen is placed slightly differently (Fig. 20.8c), the effect is lost, and in fact the middle carbon bond lengthens rather than shortens.

The results of this simple test molecule show that the C–C bond is significantly strengthened when nitrogen is substituted in the appropriate manner. The effect of shortening the sp^2 C–C bond occurs only when it is "trapped" between four nitrogen atoms. It may appear at first that this second-neighbor effect is due to the excess charge on the nitrogen atoms. However, by looking closely at the charge densities, we observe that all of the excess nitrogen charge remains localized on the N atoms. Instead, the effect of the nitrogen atoms is to push more of the *carbon* charge away from the C–N bond and over to the C–C "trapped" bond. The reason for such a transfer of charge is that the carbon π bonds cannot form in the usual sp^2 network with the nitrogen atoms, resulting in extra bonding with its carbon neighbor.

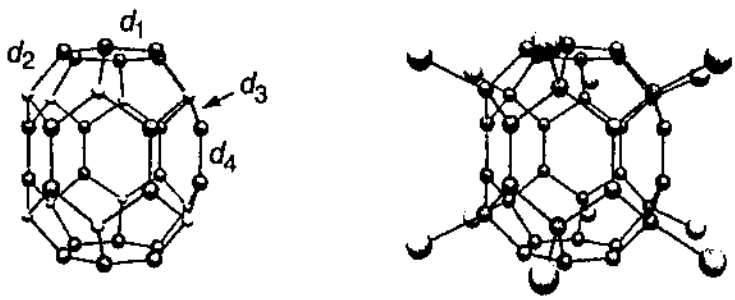

Figure 20.9 The (a) D_{6h} $C_{24}N_{12}$ fullerene and the (b) D_{6h} $C_{36}Cl_{12}$ fullerene. The four unique bonds for these structures are shown in (a).

As a further check, we have disrupted the π bonding of the 12 carbon atoms in C_{36}, which were previously substituted with nitrogen atoms by attaching additional atoms that bond to the carbons at these sites. We choose the highly electronegative Cl atoms, which pull an electron away from the carbon atoms, leaving them with a truly sp^3 bonding character. Upon structural relaxation (see Fig. 20.9b), the exact same shortening of the C–C bonds along the hexagon belt is observed. In fact, this effect has been observed experimentally for the $C_{60}Br_{24}$ compound [51], which had Br atoms situated outside the C_{60} in a tetrahedral configuration such that every C–C bond was surrounded by four C atoms attached to Br, leading to a molecule with 18 trapped C–C bonds. Thus, both substitution with nitrogen and addition of atoms, which bind to the outside of the fullerene, have the same effect on the fullerene's C–C bonds. To test this effect even further, we replaced the C atoms in C_{60} with N at exactly the positions where the Br atoms were attached in the experiment of Tebbe et al. [51]. Our calculations of the resulting $C_{36}N_{24}$ fullerene show almost identical bond lengths to those of the experimental brominated C_{60}.

It is interesting to note that the chlorination of these D_{6h} C_{36} fullerenes may be significantly easier than for C_{60} because the smaller fullerenes are more reactive. Our calculations of $C_{36}Cl_{12}$ show an energetically stable structure with a large LDA gap of 2.5 eV. In C_{60}, the addition of bromine atoms to the surface creates structural distortions that cause considerable strain on the molecule. In contrast, pure C_{36} already has some of these distortions (referred to as the "boat" conformation by Tebbe et al. [51]), so little additional geometric strain is introduced.

20.7.2 Endohedral Doping

Next, we consider endohedral doping of the molecules as an additional means of modifying their electronic properties. The detection of endohedral fullerenes

TABLE 20.5 Binding Energies, ΔE, of Endohedrally Doped Atoms in C_{36} (D_{6h} and D_{2d}) and C_{28} (T_d): $\Delta E = E(M) + E(C_{36}) - E(M@C_{36})$, Where M Is the Dopant Atom

	Mg	Ca	Ge	Si	Zr	Sr
ΔE (C_{36} D_{6h})	+0.9	+4.7	+1.2	+1.4	+6.7	+4.2
ΔE (C_{36} D_{2d})	+0.3	+4.2	+0.7	+0.9	+6.1	+4.9
ΔE (C_{28})*	−1.6	−4.5	—	−7.8	+2.8	—

*From Ref. 55.

such as La@C_{60} [52] shortly after the discovery of C_{60} led to the suggestion of encapsulating atoms inside carbon cages as a technique for creating new materials [53–55]. When an alkaline-earth atom M is placed in the center of pure C_{36}, the outer valence electrons from M jump onto the ball and fill the first LUMO, in accord with a rigid-band type model. Thus, very little changes in the electronic and structural properties of these endohedrally doped fullerenes, except perhaps the degeneracy of the LUMO or spin multiplicity.

We have evaluated the binding energies, ΔE, of various endohedral atoms as the difference of total energies, $\Delta E = E(M) + E(C_{36}) - E(M@C_{36})$, where M is the dopant atom. Results for doping with the alkaline-earth atoms Mg, Ca, and Sr for the D_{6h} and D_{2d} fullerenes are given in Table 20.5. In addition, we calculate the binding energies of Si, Ge, and Zr in order to compare with the same quantities calculated by Guo et al. [55] for C_{28}. Note that, while C_{28} binds only one of the atoms (Zr), all of the atoms that we tried are well-bounded by the C_{36} cages. Thus, the C_{36} fullerenes are perhaps the smallest size carbon cages that easily trap additional atoms.

20.7.3 Intercalation in the Solid

Upon closer inspection of Figure 20.6, we observe that in the S2-AB crystal there are two cavities per C_{36} (directly above and below each molecule), which have a radius of roughly 1.4 Å. These are the largest empty spaces and would therefore be appropriate for intercalation with alkali metal atoms. The ionic radii of Na and K are 0.95 and 1.33 Å, respectively, indicating that Na should fit well but that perhaps K is too large.

In order to test the effects of these dopants, we have carried out calculations of the S2-AB crystal with both Na and K intercalated at the above-mentioned sites (two metal atoms per C_{36}). Relaxed structures of both Na- and K-doped crystals are shown in Figure 20.10. Note that Na_2C_{36} maintains the original crystal structure and little relaxation occurs upon introducing the intercalant. In contrast, K_2C_{36} is highly strained in the original crystal and therefore undergoes a structural transition. In this case, the top and bottom hexagons of each C_{36} molecule are "opened up" in order to relieve the strain of accommodating the large K atom, and intermolecular bonds within the planes are broken as the C_{36} molecules push away from one another.

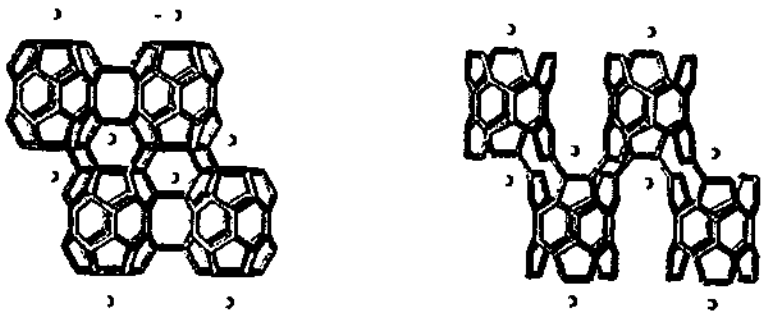

Figure 20.10 Na_2C_{36} and K_2C_{36} crystal structures. Before relaxation, both crystals appear the same; upon relaxation the K-doped crystal undergoes a structural transition.

Our results for the density of states of the Na_2C_{36} crystal (Fig. 20.11) show that the two electrons per C_{36} donated by the Na atoms fill the empty band above E_F of the undoped crystal in a rigid-band manner. There is some broadening of this band, although a small gap of ~0.2 eV remains in the crystal. Further doping of the S2-AB crystal by one or even more alkali atoms should result in a partially filled peak at E_F. While K_2C_{36} forms a very interesting crystal structure, our results demonstrate that fabrication of C_{36}-based

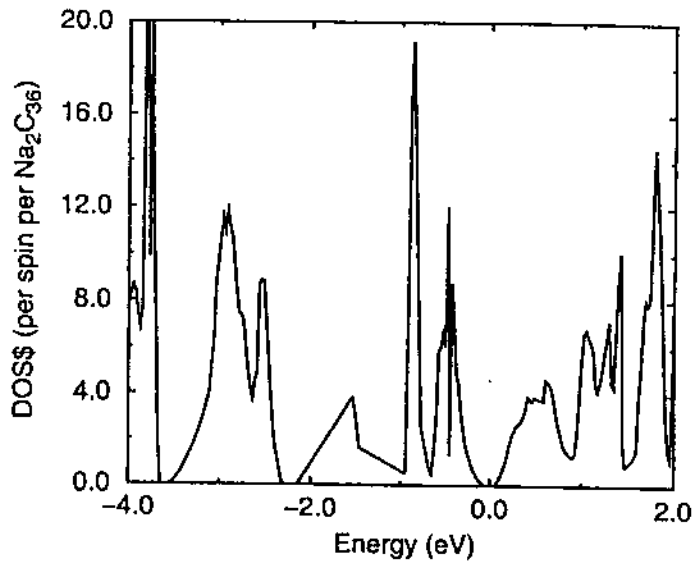

Figure 20.11 Calculated density of states (DOSs) for the alkali-doped Na_2C_{36} in the S2-AB crystal structure. The Fermi energy is at 0 eV.

superconductors with K would require the C_{36} molecules to be well separated at the time of intercalation.

20.8 FURTHER MOLECULAR PROPERTIES

20.8.1 Chemical Shifts

An experimental determination of the fullerene structures is not feasible with mobility measurements since the fullerene drift times cannot be separated out. On the other hand, NMR chemical shifts distinguish atoms in different chemical environments and could be used if the bonding configurations of the nonequivalent atoms of the C_{36} fullerenes differ enough. We have performed NMR calculations for the D_{6h} and D_{2d} structures using the gauge-independent atomic orbital (GIAO) method [56,57] with cc-pVTZ basis sets [58].

The chemical shifts are computed with respect to methane at 0 K (r_e = 1.087) and it was assumed that δ_{TMS} (CH_4) = −14.3 ppm [59]. Our results are shown in Table 20.6, which lists the isotropic chemical shift with respect to TMS for the two fullerenes. For the D_{6h} structure two of the three nonequivalent atoms have nearly identical shifts, which should cause a large peak at around 159–160 ppm. For the D_{2d} structure, the five peaks are clearly identifiable, and one can therefore distinguish between these two fullerenes due to the different numbers of identifiable peaks.

20.8.2 Infrared Spectra

To further test the possibility of distinguishing between the D_{6h} and D_{2d} molecules, we have performed calculations of IR modes using the Gaussian94 package [60] with the S-VWN5 option (Slater exchange and Vosko–Wilks–Nusair parameterization of the correlation functional) and 6-311G* basis set.

TABLE 20.6 Calculated NMR Chemical Shifts (ppm) Relative to Tetramethylsilane (TMS) for C_{36} Fullerenes with D_{6h} and D_{2d} Symmetries[a]

Molecule	Atom	δ_{TMS}	Intensity
C_{36} (D_{6h})	C1	137.5	1/3
	C2	159.4	1/3
	C3	160.0	1/3
C_{36} (D_{2d})	C1	151.8	1/9
	C2	160.5	2/9
	C3	150.3	2/9
	C4	139.3	2/9
	C5	135.7	2/9

[a]Symmetry unique atoms (see Fig. 20.1) and intensities are also listed.

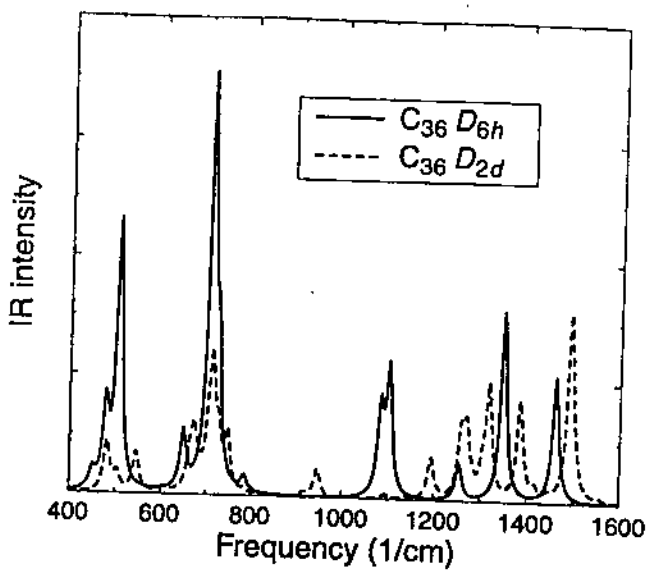

Figure 20.12 LDA calculated IR spectra for the D_{6h} and D_{2d} molecules.

The relative absorption intensities of the different modes are also computed by evaluating the effective-charge tensor, which permits the calculation of the induced dipole due to the motion of the atoms. We perform such calculations for both the D_{6h} and D_{2d} isomers at fully relaxed LDA geometries. The results for the fundamental infrared absorption, represented by upward peaks, are shown in Figure 20.12.

The calculated intensities show that we expect somewhat stronger absorption for the D_{6h} structure than for the D_{2d} structure. This result implies that if the two structures are present in the sample, the D_{2d} structure might not be able to be resolved. From the symmetry of the different molecules we can deduce that the D_{6h} fullerene has 13 IR active modes and the D_{2d} has 37 IR active modes, but only a few of those have significant absorption intensities. Note that only the D_{6h} structure has a significant peak near 1100 cm^{-1}. This observation provides additional support to the idea that experimental characterization can allow one to distinguish between the two different fullerenes.

20.9 EXPERIMENTS

20.9.1 Synthesis

A method of synthesizing C_{36} has been developed using a carbon arc discharge method and preliminary results suggest that it is a closed-cage, fullerene-like structure [8]. Six millimeter (dc) POCO graphite rods were arced together using a 100 ampere direct current source in a 400 torr helium atmosphere. The arc

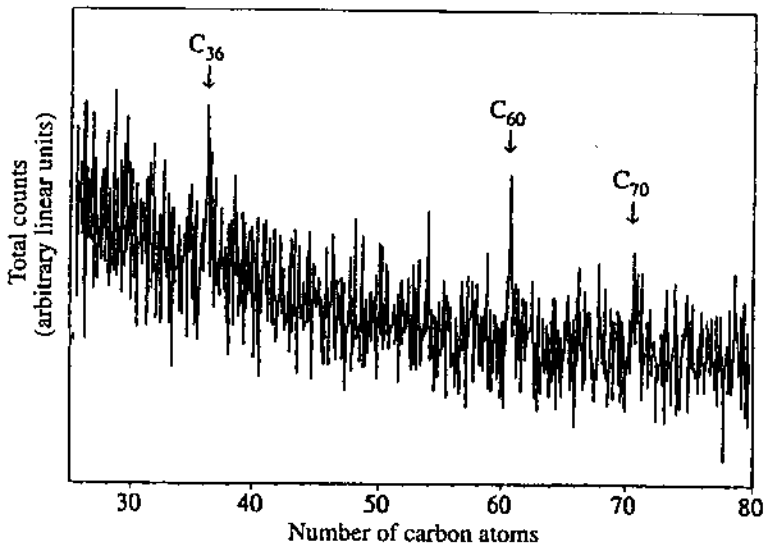

Figure 20.13 Time-of-flight mass spectrum of a sample of crude fullerene soot produced at a helium pressure of 400 torr. The data show the presence of a peak at the mass of C_{36} (432 amu) with approximately the same intensity as the peak due to C_{60} (720 amu).

chamber apparatus was similar to that described by Krätschmer et al. [3]. Films produced by the graphite sublimation were grown directly onto a probe head for use in a micromass time-of-flight mass spectrometer using a 366 nm nitrogen laser for desorption and ionization of the sample. All spectra were taken in negative ion mode. Figure 20.13 shows the mass spectrum of one of these films grown at 400 torr helium. The dominant peaks in the spectrum are at 720 and 432 amu. The former peak corresponds to 60 carbon atoms, while the latter corresponds to 36 carbon atoms. The C_{60} and C_{36} peaks are of comparable magnitude and these molecular species appear to be the most prominent in the sample. Lesser peaks are also observed, for example, at 840 amu (C_{70}). The synthesis of C_{36} is very sensitive to experimental conditions, notably the helium pressure: Runs in this series at pressures significantly different from 400 torr failed to produce prominent peaks below 720 amu in the mass spectrum.

To produce bulk amounts of C_{36} suitable for purification, arcing runs at 400 torr helium were repeated and the resulting "soot" was collected from the synthesis chamber walls. To avoid possible reactions with atmospheric impurities, the samples were removed from the arc chamber and handled inside an argon atmosphere glovebox. The soot was initially washed with toluene in a standard Soxhlet extractor, which removed C_{60}, C_{70}, and trace amounts of even higher-order fullerenes. Mass spectrometry on the toluene-soluble extract showed the expected fullerene peaks but no peak at 432 amu, indicating that C_{36} is not soluble in toluene. Next, the sublimation product was extracted with pyridine.

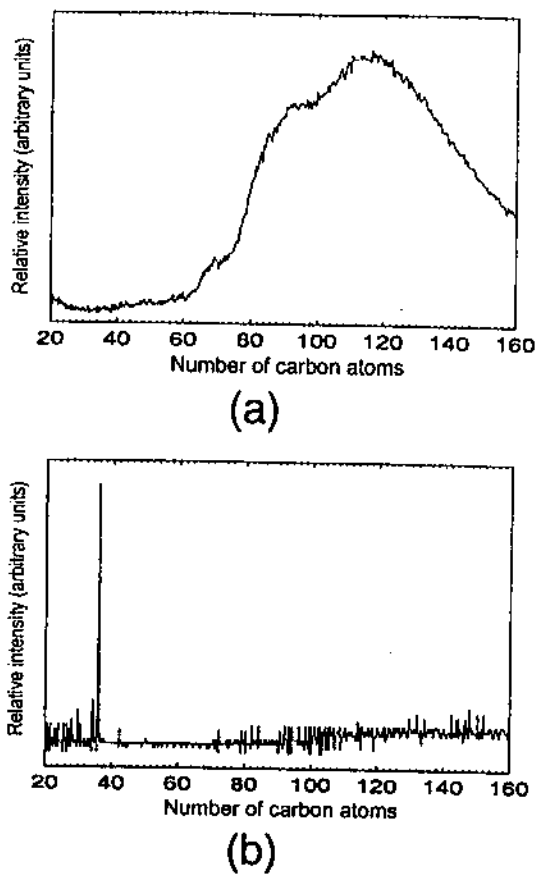

Figure 20.14 (a) Time-of-flight mass spectrum of the pyridine-soluble extract from higher fullerene depleted soot. (b) Time-of-flight mass spectrum of the same material after reduction with potassium metal in liquid ammonia.

This pyridine-soluble fraction formed a dark yellow solution as opposed to the toluene-soluble fraction, which was dark red.

Mass spectrometry of this fraction produced the spectrum shown in Figure 20.14a. Here, a very broad mass distribution is observed, which peaks at about 1500 amu. A similar spectrum has been published previously and attributed to the presence of higher fullerenes [61]. However, Figure 20.14b shows a mass spectrum of the same material after a subsequent reduction with one molar equivalent of potassium stirred for 3 hours in liquid ammonia and then dried. This spectrum shows only one major peak at C_{36} and almost no signal in the higher mass region around 1500 amu [62]. One possible explanation of this difference in spectra is that the pyridine extract is composed of covalently bonded C_{36} solid particles, which fragment upon laser desorption, producing

species composed of 100–140 carbon atoms. However, potassium reacts with the material by transferring electrons to the molecules, thereby reducing the intermolecular binding energy and allowing individual molecules to desorb from the surface. This material was also found to dissolve in carbon disulfide (CS_2) and liquid ammonia.

20.9.2 Electron Diffraction

Electron diffraction studies were performed on the solid C_{36} obtained from the pyridine extraction. A small amount of the material was ground up, dispersed on a holey carbon grid, and inserted into a JEOL 200CX transmission electron microscope (TEM). The material was observed to be polycrystalline with a crystallite grain size of about 100 nm. Using a field-limiting aperture, the diffraction pattern of selected crystallites was recorded.

Figure 20.15 shows a TEM diffraction pattern for a C_{36} crystallite. The hexagonal diffraction pattern suggests a close-packing arrangement perpendicular to the zone axis. The pattern is reminiscent of diffraction patterns observed for C_{60} and C_{70}. However, the *d*-spacing measured from this pattern for the first-order diffracted spots is 6.68 Å, significantly less than the (100) *d*-spacing of 8.7 Å reported for C_{60}. This *d*-spacing is consistent with the predicted *d*-

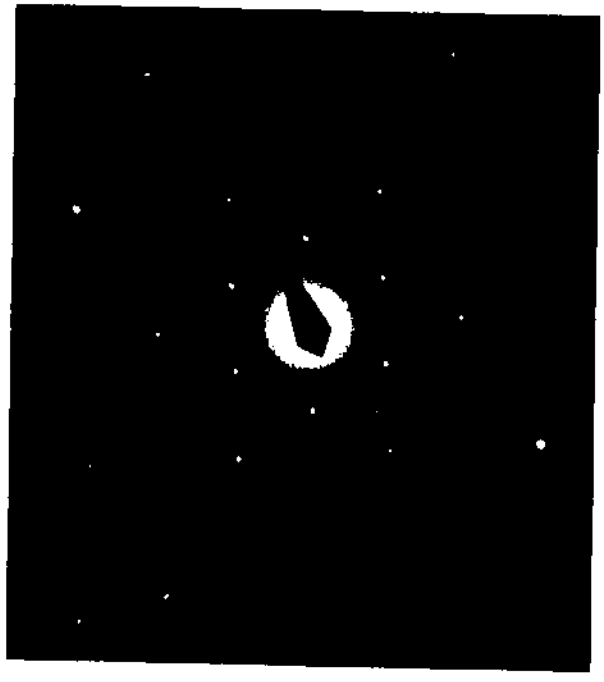

Figure 20.15 Electron diffraction pattern of C_{36} crystallite. The pattern is hexagonal with a calculated *d*-spacing of 6.68 Å.

spacing of 6.55 Å for the lowest energy S2-AB C_{36} crystal structure (see Section 20.5). Unfortunately, because the C_{36} crystallites are platelets with high aspect ratios, this was the only zone axis along which the crystallites were thin enough to allow useful TEM imaging, and thus determination of the detailed C_{36} crystal structure was not possible.

Like C_{60}, C_{36} appears to suffer some TEM-induced damage at an electron beam energy of 200 keV. Under continuous TEM observation, the sharp crystalline diffraction patterns were found to deteriorate for extended irradiation times. Additional studies were performed to investigate the long-term stability of solid C_{36} subject (only) to high ambient temperatures. C_{36} powder was heated in vacuum to 1350 °C for 48 hours and then characterized by TEM imaging. Over 50% of the diffraction patterns obtained for the heat-treated material were graphitic, indicating that a large amount of the material had converted to the energetically more favorable graphite.

20.9.3 Scanning Tunneling Spectroscopy

The molecular energy levels of C_{36} thin films have also been studied by scanning tunneling spectroscopy (STS) [9]. The measured local density of electronic states $N(E)$ has been compared to a predicted density of states for the C_{36} monomer as well as several C_{36} dimer and trimer configurations. C_{36} films were grown using two separate methods—thermal evaporation and solution deposition. For thermal evaporation, the pyridine-soluble extract described in Section 20.9.1 was dried and thermally evaporated from a tungsten filament at approximately 10^{-6} torr onto a substrate, which was suspended above the filament. In order to prevent thermal decomposition of the material, the filament was heated very quickly and the films were grown in a matter of seconds. A shutter was used between the source and the substrate to control the film thickness. Films with thicknesses on the order of 0.1 monolayer to 1 monolayer were grown. Alternatively, films were grown by simply depositing a dilute solution of the pyridine extract onto the substrate and allowing the solvent (carbon disulfide) to evaporate. Two substrates were used in this study—an atomically flat gold (111) film grown on mica and the (001) surface of a highly oriented pyrolytic graphite (HOPG) crystal.

Each of these films were immediately loaded into a room temperature scanning tunneling microscope (STM) using a Pt-Ir tip and Oxford instruments TOPS3 controller. For all samples it was found that the C_{36} film tended to aggregate into islands approximately 10–50 nm in diameter and 10–20 Å high. This clustering is consistent with the predicted tendency of these molecules to covalently bind together. Figure 20.16 shows the STS density of states $((V/I)dI/dV)$ plot versis tip bias voltage obtained by placing the tip at a fixed height above a C_{36} island for both substrates. A similar measurement performed above the clean substrates produced the flat line at zero on this plot. Here, several sharp peaks can be seen, which indicate resonant tunneling through discrete molecular states. No differences between the thermally evapo-

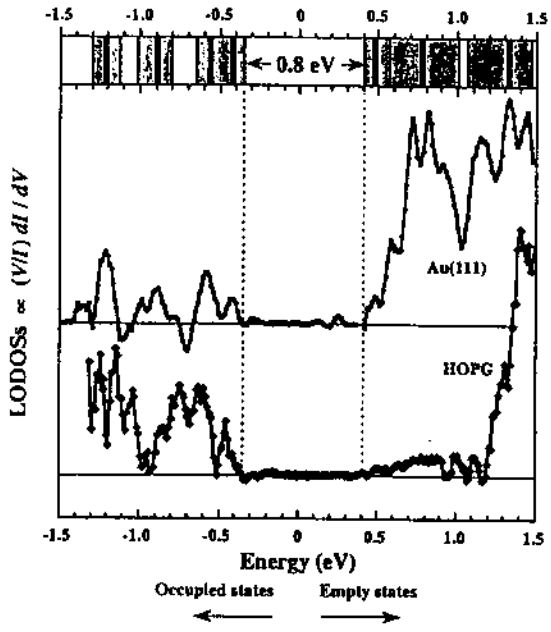

Figure 20.16 $N(E)$ for C_{36} as measured on Au (111) and HOPG substrates. The most reproducible states on both substrates are indicated at the top by black lines with the measured broadening shown in gray.

rated films and the solution grown films could be found. Both spectra indicate the presence of a 0.8 eV gap. There appears to be a slight discrepancy in the features of these graphs, which may be explained by the possibility that the surface is influencing the electronic structure of the clusters. Nevertheless, the features that are most reproducible on both substrates have been indicated by black strips at the top of the figure with the peak widths shown in gray.

Our theoretical LDA calculations for isolated D_{6h} symmetry C_{36} molecules compare favorably with these results and are reproduced at the top of Figure 20.17. After accounting for the standard LDA underestimation of the energy gap, the experimental and theoretical spectra match closely near the Fermi level. The theoretical energy spacing between the two lowest unoccupied and two highest occupied molecular levels, as well as the relative spectral weights of these levels, are all reproduced by the experimental data.

However, there is serious disagreement between experiment and theory further from the Fermi level: In the LDA, the isolated molecule has no eigenvalues in the +1.0 to +2.0 eV and the −1.0 to −2.0 eV energy ranges, while a number of states appear to be present experimentally. There are a number of effects that may explain such a discrepancy, including (1) bonding between C_{36} units, (2) impurities in the sample, and (3) passivation of the C_{36} molecules by other species. As we have already discussed, C_{36} molecules are predicted to be more

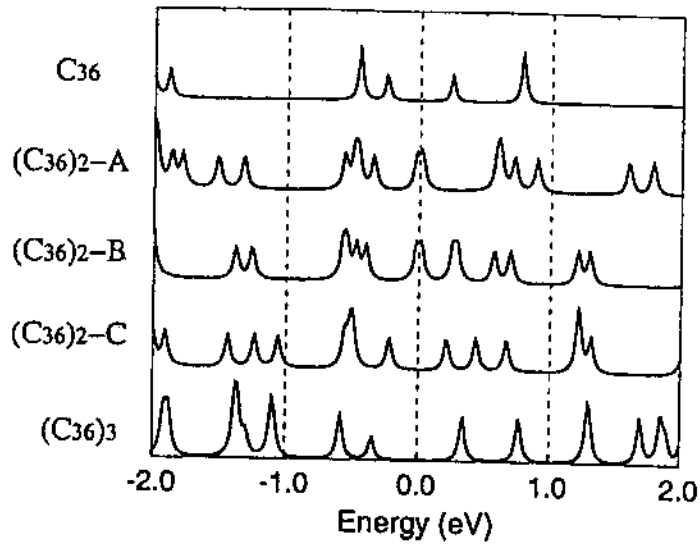

Figure 20.17 Theoretical electronic spectra for five different configurations of C_{36} molecules illustrated in Figure 20.3. $(C_{36})_2$-C and $(C_{36})_3$ provide the best match for the experimental spectrum.

reactive than larger fullerenes like C_{60}, even to the extent that stable covalently bonded crystals may be formed. Although impurities and passivation cannot absolutely be ruled out, the vacuum environment in which the samples were produced would favor intermolecular bonding as the most likely cause of deviation from isolated-molecule behavior, particularly considering that the molecules are mobile enough to cluster into islands.

To investigate the possible effects of intermolecular bonding, we have also calculated the energy spectra for the dimers and the trimer we considered earlier (see Section 20.4). The resulting molecular orbital energy spectra shown in Figure 20.17 indicate how sensitive the eigenvalue spectrum is to the nature of the intermolecular bonding. To facilitate comparison with the experimental results, a small, unweighted Lorentzian broadening is employed and each spectrum has been shifted so that the middle of the HOMO–LUMO gap lies at 0 eV. Doubly degenerate levels are counted twice so that relative peak heights are meaningful. In dimers A and B, a small gap (0.01 eV) results in a metallic eigenvalue spectrum. Dimer C, on the other hand, has a gap that is roughly the same as in the isolated molecule, shown at the top of the figure.

The experimental data in Figure 20.16 may now be compared directly to the various theoretical spectra of Figure 20.17. Neither dimers A nor B have the appropriate gap, as found for the isolated C_{36} molecule or dimer C. Although the isolated molecule fits the experimental data reasonably well, as described earlier, dimer C possesses a more even distribution of states in the range of 1–2 eV above and below the Fermi level. This particular dimer, therefore, resolves

the primary discrepancy between the experimental data and the isolated-molecule energy spectrum. Since it is also considerably well bound energetically, it strongly suggests that the C_{36} molecules are dimerized rather than isolated in this study.

ACKNOWLEDGMENTS

We thank M. Côté for significant contributions to the theoretical portion of this work, and K. Bradley, J. Burward-Hoy, P. G. Collins, M. Ishigami, T. Wagberg, M. C. Martin, Lafe Spietz, J. Kriesel, T. D. Tilley, J. Yarger, M. Tomaselli, and A. Pines for aiding in the synthesis and experimental investigation of this material. Support for this work was provided by the National Science Foundation, Grant No. DMR-9404755, and the Director, Office of Energy Research, Office of Basic Energy Sciences, Material Sciences Division of the U.S. Department of Energy under Contract Number DE-AC-03-76SF00098. Computational resources have been provided by NCSA, by SDSC, and by NERSC.

REFERENCES

1. H. W. Kroto, J. R. Heath, S. C. O'Brien, R. F. Curl, and R. E. Smalley, *Nature* 1985, *318*, 162.
2. H. Ehrenreich and F. Spaepen (eds), *Solid State Physics: Advances in Research and Applications*. Academic Press, San Diego, 1994.
3. W. Krätschmer, L. D. Lamb, K. Fostiropoulos, and D. R. Huffman, *Nature* 1990, *347*, 354–358.
4. H. W. Kroto, *Nature* 1987, *329*, 529.
5. J. C. Grossman, M. Côté, S. G. Louie, and M. L. Cohen, *Chem. Phys. Lett.* 1998, *284*, 344.
6. M. Côté, J. C. Grossman, S. G. Louie, and M. L. Cohe, *Phys. Rev. Lett.* 1998, *81*, 697.
7. M. Côté, J. C. Grossman, M. L. Cohen, and S. G. Louie, in *Proceedings 193rd Meeting of the Electrochemical Society*, San Diego, CA, 1998.
8. C. Piskoti, J. Yarger, and A. Zettl, *Nature* 1998, *393*, 771.
9. P. G. Collins, J. C. Grossman, M. Côté, M. Ishigami, C. Piskoti, S. G. Louie, M. L. Cohen, and A. Zettl, *Phys. Rev. Lett.* 1999, *82*, 165.
10. J. C. Grossman, S. G. Louie, and M. L. Cohen, *Phys. Rev. B.*, vol. 60, num. 10, R6941 (1999).
11. See, for example, W. E. Billups and M. A. Ciufolini (eds.), *Buckminsterfullerenes*. VCH Publishers, New York, 1993.
12. E. A. Rohlfing, D. M. Cox, and A. Kaldor, *J. Chem. Phys.* 1984, *81*, 3322.
13. S. C. O'Brien, J. R. Heath, R. F. Curl, and R. E. Smalley, *J. Chem. Phys.* 1988, *88*, 220.

14. M. L. Cohen, *Phys. Scr.* **1982**, *T1*, 5.
15. P. Hohenberg and W. Kohn, *Phys. Rev. B* **1964**, *136*, 864.
16. W. Kohn and L. J. Sham, *Phys. Rev. A* **1965**, *140*, 1133.
17. D. M. Ceperley and B. J. Alder, *Phys. Rev. Lett.* **1980**, *45*, 566.
18. J. L. Martins, N. Troullier, and S.-H. Wei, *Phys. Rev. B* **1991**, *43*, 2213.
19. H. J. Monkhorst and J. D. Pack, *Phys. Rev. B* **1976**, *13*, 5188.
20. B. Delley, *J. Chem. Phys.* **1990**, *92*, 508.
21. S. H. Vosko, L. Wilk, and M. Nusair, *Can. J. Phys.* **1980**, *58*, 1200.
22. J. P. Perdew, in *Electronic Structure of Solids '91*, P. Ziesche and H. Eschrig (eds.). Akademie Verlag, Berlin, 1991, p. 11.
23. A. D. Becke, *J. Chem. Phys.* **1993**, *98*, 5648.
24. G. von Helden, M. T. Hsu, N. G. Gotts, and M. T. Bowers, *J. Phys. Chem.* **1993**, *97*, 8182.
25. L. D. Book, C. Xu, and G. Scuseria, *Chem. Phys. Lett.* **1994**, *222*, 281.
26. P. W. Fowler and D. E. Manolopoulos, *An Atlas of Fullerenes*. Clarendon Press, Oxford, 1995.
27. M. Feycreisen, M. Gutowski, J. Simons, and J. Almlof, *J. Chem. Phys.* **1992**, *96*, 2926.
28. K. Raghavachari, D. L. Strout, G. K. Odom, G. E. Scuseria, J. A. Pople, B. G. Johnson, and P. M. W. Gill, *Chem. Phys. Lett.* **1993**, *214*, 357.
29. J. C. Grossman, L. Mitas, and K. Raghavachari, *Phys. Rev. Lett.* **1995**, *75*, 3870.
30. D. Bakowies and W. Thiel, *J. Am. Chem. Soc.* **1991**, *113*, 3704.
31. D. Bakowies, A. Gelessus, and W. Thiel, *Chem. Phys. Lett.* **1992**, *197*, 325.
32. R. C. Haddon, *Science* **1993**, *261*, 1545.
33. G. B. Adams, J. B. Page, O. F. Sankey, and M. O'Keeffe, *Phys. Rev. B* **1994**, *50*, 17471.
34. J. Kürti and K. Németh, *Chem. Phys. Lett.* **1996**, *256*, 119.
35. J. Fagerström and S. Stafström, *Phys. Rev. B* **1996**, *53*, 13150.
36. M. E. Colvin, N. L. Trian, L. L. Bui, J. C. Grossman, S. G. Louie, M. L. Cohen, and C. Janssen, *Chem. Phys. Lett.*, submitted.
37. J. L. Martins, *Europhys. News* **1992**, *23*, 31.
38. M. Schluter, M. Lannoo, M. Needels, and G. A. Baraff, *Phys. Rev. Lett.* **1992**, *68*, 526.
39. P. B. Allen and B. Mitrović, *Solid State Phys.* **1982**, *37*, 2–91.
40. C. M. Varma, J. Zaanen, and K. Raghavachari, *Science* **1991**, *254*, 989.
41. O. Gunnarsson, H. Handschuh, P. S. Bechthold, B. Kessler, G. Ganteför, and W. Eberhardt, *Phys. Rev. Lett.* **1995**, *74*, 1875.
42. S. J. Duclos, R. C. Haddon, S. Glarun, A. F. Hebard, and K. B. Lyons, *Science* **1991**, *254*, 1625.
43. T. Pichler, M. Matus, J. Kürti, and H. Kuzmany, *Phys. Rev. B* **1992**, *45*, 13841.
44. V. P. Antropov, O. Gunnarsson, and A. I. Liechtenstein, *Phys. Rev. B* **1993**, *48*, 7651.
45. J. C. R. Faulhaber, D. Y. K. Ko, and P. R. Briddon, *Phys. Rev. B* **1993**, *48*, 661.

46. M. S. Fuhrer, K. Cherrey, V. H. Crespi, A. Zettl, and M. L. Cohen, Physical Review Letters. 1999, Vol. 83 p. 404–407.
47. T. Guo, C. Jin, and R. E. Smalley, *J. Phys. Chem.* **1991**, *95*, 4948.
48. S. Glenis, S. Cooke, X. Chen, and M. M. Labes, *Chem. Mater.* **1994**, *6*, 1850.
49. W. Andreoni, F. Gygi, and M. Parrinello, *Chem. Phys. Lett.* **1991**, *190*, 159.
50. X. Xia, D. A. Jelski, J. R. Bowser, and T. F. George, *J. Am. Chem. Soc.* **1992**, *114*, 6493.
51. F. N. Tebbe, R. L. Harlow, D. B. Chase, D. L. Thorn, G. C. Campbell, Jr., J. C. Calabrese, N. Herron, R. J. Young, and E. Wasserman, *Nature* **1992**, *256*, 822.
52. J. R. Heath, S. C. O'Brien, Q. Zhang, Y. Liu, R. F. Curl, H. W. Kroto, F. K. Tittel, and R. E. Smalley, *J. Am. Chem. Soc.* **1985**, *107*, 7779.
53. S. D. Bethune, R. D. Johnson, J. R. Salem, M. S. de Vries, and C. S. Yannoni, *Nature* **1993**, *366*, 123.
54. T. Guo, M. D. Diener, Y. Chai, M. J. Alford, R. E. Haufler, S. M. McClure, T. Ohno, J. H. Weaver, G. E. Scuseria, and R. E. Smalley, *Science* **1992**, *257*, 1661.
55. T. Guo, R. E. Smalley, and G. E. Scuseria, *J. Chem. Phys.* **1993**, *99*, 352.
56. K. Wolinski, J. F. Hilton, and P. Pulay, *J. Am. Chem. Soc.* **1990**, *112*, 8251.
57. J. L. Dodds, R. McWeeny, and A. J. Sadlej, *Mol. Phys.* **1980**, *41*, 1419.
58. T. H. Dunning, Jr., *J. Chem. Phys.* **1989**, *90*, 1007.
59. A. K. Jameson and C. J. Jameson, *Chem. Phys. Lett.* **1987**, *134*, 461.
60. M. J. Frisch et al., *GAUSSIAN94, Revision B.1*. Gaussian, Inc., Pittsburgh, PA, 1995.
61. K. R. Lykke, D. H. Parker, and P. Wurz, *Int. J. Mass Spectrometry Ion Processes* **1994**, *138*, 149–157.
62. M. L. Cohen, J. C. Grossman, S. G. Louie, C. Piskoti, A. Zettl, *Electronic Properties of Novel Materials – Science and Technology of Molecular Nanostructures*, edited by H. Kuzmany, J. Fink, M. Mehring, & S. Roth © 1999 American Institute of Physics p. 183–186. "Effect of Alkali Doping on the Structural Stability of Solid C_{36}".